Analysis of thermomechanical behaviour in billet casting with different mould corner radii

J. K. Park, B. G. Thomas, and I. V. Samarasekera

A finite element thermal stress model to compute the thermomechanical state of the solidifying shell during continuous casting of steel in a square billet casting mould has been applied to investigate longitudinal cracks. A two-dimensional thermoelastoviscoplastic analysis was carried out within a horizontal slice of the solidifying strand which moves vertically within and just below the mould. The model calculates the temperature distributions, the stresses, the strains in the solidifying shell, and the intermittent air gap between the casting mould and the solidifying strand. Model predictions were verified with both an analytical solution and a plant trial. The model was then applied to study the effect of mould corner radius on longitudinal crack formation for casting in a typical 0·75%/m tapered mould with both oil and mould powder lubrication. With this inadequate linear taper, a gap forms between the shell and the mould in the corner region. As the corner radius of the billet increases from 4 to 15 mm, this gap spreads further around the corner towards the centre of the strand and becomes larger. This leads to more temperature non-uniformity around the billet perimeter as solidification proceeds. Longitudinal corner surface cracks are predicted to form only in the large corner radius billet, owing to tension in the hotter and thinner shell along the corner during solidification in the mould. Off corner internal cracks form more readily in the small corner radius billet. They are caused by bulging below the mould, which bends the thin, weak shell around the corner, creating tensile strain on the solidification front where these longitudinal cracks are ultimately observed. I&S/1675

Dr Park is at the University of British Columbia, 141–2355 East Mall, Vancouver, BC, Canada, Professor Thomas (bgthomas@uiuc.edu) is in the Department of Mechanical and Industrial Engineering, University of Illinois at Urbana–Champaign (UIUC), 1206 W Green Street, Urbana, IL, 61801, USA, and Professor Samarasekera is in the Department of Metals and Metallurgical Engineering, University of British Columbia, 111–2355 East Mall, Vancouver, BC, Canada.
Manuscript received 27 February 2002; accepted 16 July 2002.

INTRODUCTION

During the continuous casting of steel billets, the corner regions of the cast section often experience local thinning. This phenomenon, sometimes referred to as 're-entrant corners', results from the complex behaviour of the air gap, which forms between the mould and the solidifying shell in the corner region. This common occurrence can lead to problems such as longitudinal cracks near the billet corner, especially at high casting speed.[1–3] In extreme cases, the corners may be so thin that a breakout occurs, even though the average shell thickness is easily large enough to withstand the ferrostatic pressure at the mould exit.

Two decades of operating experience have shown that reducing the corner radius from 12–16 mm to 3 or 4 mm is beneficial in reducing longitudinal corner cracking.[4] In addition to lessening crack frequency, decreasing the corner radius also tends to move the crack location from the corner itself to the off corner region. Unfortunately, billets with sharp edges tend to 'fold over' during the rolling process.[5] Therefore, mould designers struggle to satisfy these two conflicting requirements. A better way to solve the longitudinal corner crack problems is desirable. An important step towards this end is the achievement of an accurate, quantitative understanding of the crack formation mechanism(s). This understanding would aid mould design optimisation, especially for high speed casting.

Over the years, many mathematical models have been developed to help to understand the origin of defects in complex processes such as continuous casting.[6–11] However, quantitative understanding of the re-entrant corner phenomenon of the solidifying shell in the billet mould has received relatively little attention. Furthermore, the effect of the billet mould corner radius on the temperature, corner gap, and stress development has not been studied.

In the present work, a thermal–elastic–plastic–creep finite element model has been developed to study the thermal–mechanical behaviour of the solidifying shell in and just below a billet mould. The model was validated with plant measurements including solid shell thickness and mould thermocouple temperatures. The model was then applied to the re-entrant corner phenomenon to investigate the influence of corner radius on longitudinal crack formation.

PREVIOUS WORK

Longitudinal cracks

Longitudinal cracks are one of the most common mould related quality problems encountered in billet casting. They are associated with hot tearing close to the solidification front,[2] and are manifested in at least two different forms: 'longitudinal corner cracks' and 'off corner internal cracks'.

Longitudinal corner cracks run along the surface near the exact corner of the billet and are usually 1–2 mm in depth,[12] as shown in Fig. 1*a*. Although several studies suggest that longitudinal corner cracks are related to the rhomboid condition of the billet,[12,14–17] these cracks also occur in the absence of rhomboidity, as a result of improper corner radius [12,18] or mould distortion and wear.[14,15] Aketa and Ushijima[18] observed that with a large corner radius, the longitudinal corner cracks appear along the corner, while with smaller radii, these surface cracks form more frequently at the off corner region. They suggested that the optimal corner radius to minimise longitudinal crack formation should be one-tenth of the section size.[2] However, Samarasekera and Brimacombe[12] believed that the modern trend of smaller corner radii such as 3 or 4 mm may solve the longitudinal corner cracking problem, but at the expense of creating more off corner cracks. Mori[15] observed that the incidence of longitudinal corner cracks increases with the time that a mould is in service during a campaign. He suggested that overall reverse of taper may be an important

DOI 00.0000/000000000000000000

ias0001675 23-09-02 11:50:50 Rev 14.05
The Charlesworth Group, Huddersfield 01484 517077

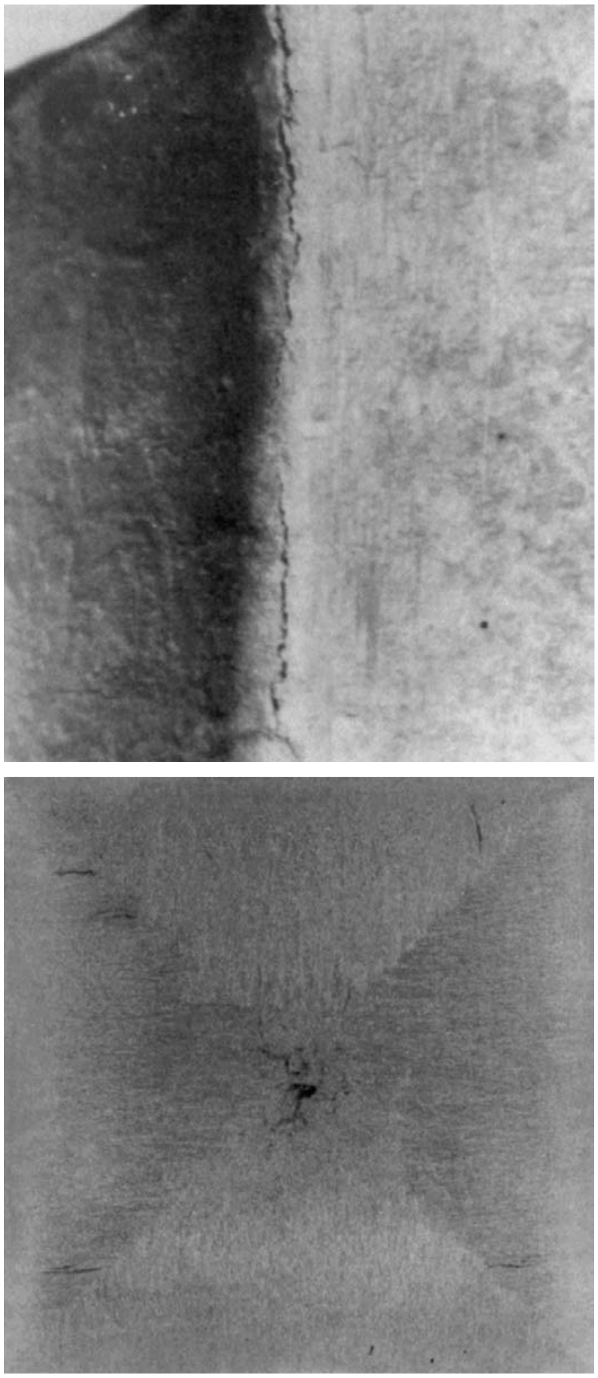

a longitudinal corner crack; *b* off corner internal cracks

1 Appearance of longitudinal cracks in billet casting[12,13]

contributor. This was attributed to permanent creep distortion of the upper mould towards the steel, and wear in the lower mould with longer service time.

Although longitudinal corner cracks are believed to form in the mould,[2,5] off corner internal cracks are believed to form below the mould in the spray cooling zone.[3] These cracks,[13] shown in Fig. 1*b*, are located ~15 mm from a given corner starting at a depth of 4–11 mm from the billet surface and extending to a depth of 13–20 mm.[3,12] By analysing the microstructure of a billet obtained from industrial trials using heat flow calculations, Brimacombe *et al.*[3] deduced that cracks can form as a result of bulging of the solid shell in the lower part of the mould. They proposed that as bulging occurs, a hinging action develops near the cold and strong corners, causing off corner tensile stresses near the solidification front, and cracking. The cause of the shell bulging was guessed to be thermal distortion or wear in the lower region of the mould. This bulging could arise if improperly set foot rolls or wobbling of the mould during its oscillation cycle causes the strand to move about in the lower region of the mould.

Mathematical stress models

During continuous casting, solidification of the steel shell in the mould region involves many complex phenomena such as fluid flow, interaction of shrinkage of the shell and ferrostatic pressure, which leads to intermittent contact with the mould, and interaction of interfacial heat transfer with air gap formation. Over the years, many mathematical models have investigated the thermal and mechanical behaviour of the solidifying shell with air gap formation in the continuous casting of steel in a billet mould.[6–11]

Grill *et al.*[6] applied an elastic–plastic model of the billet strand to study its thermomechanical behaviour and to explain internal crack formation. They calculated the heat transfer coefficient in the corner region and were able to predict corner cracks in the billet by coupling heat flow to the air gap computed from stress analysis. The model was improved later by Sorimachi and Brimacombe[7] with better material property data. They observed that internal cracks could be caused by surface reheating below the mould.

Kristiansson and Zetterlund[8,9] simulated billet casting using a stepwise coupled two-dimensional thermal and mechanical model, which also calculated the size of the shell–mould gap around each portion of the strand periphery at each time. The model was applied to investigate the formation of longitudinal subsurface cracks in the solidifying shell. They suggested that large air gaps, which may form owing to wear or misalignment of the mould, cause large strains in the solidifying shell and a high risk of cracking.

Kelly *et al.*[10] developed a coupled two-dimensional axisymmetric thermomechanical model for steel shell behaviour in round billet casting moulds using a combination of models FIDAP and NIKED2D. Their model was fully coupled through the interface gap, included mould distortion, and assumed elastic–plastic mechanical behaviour. Their results suggested that thermal shrinkage associated with the phase change from δ ferrite to austenite in 0·1%C steel accounts for the decreased heat transfer observed in this alloy as well as its susceptibility to cracking.

Tszeng *et al.*[11] calculated billet temperature fields using a temperature recovery solidification method, followed by an uncoupled stress analysis with plane strain in the MARC model. They interpreted the results to obtain qualitative ideas about possible billet defects.

Ohnaka and Yashima[19] studied the effect of mould taper and mould corner radii on the temperature and stress fields in slab casting using an elastoplastic model, which considered the ferrostatic pressure, mould taper, and interaction between the solidifying shell and mould. This model demonstrated that shell deformation owing to thermal stress and ferrostatic pressure changes the shell–mould thermal resistance, resulting in tensile stress near the slab corner, which may cause longitudinal cracks. They also suggested that a larger mould corner radius should decrease the interfacial gap thickness and tensile stress in the shell and thereby help to prevent cracks.

In the present work, a thermoelastoviscoplastic finite element model has been developed to simulate temperature and stress in a transverse slice through the solidifying shell of a typical billet caster. The evolution of the air gap has been calculated from the deformation of the strand and the tapered and distorted mould. Its coupled effect on the temperature distribution has been taken into account with a distance dependent heat transfer coefficient between the mould and strand. The accuracy of the two-dimensional (2D) slice model formulation in this analysis has also been

ias0001675 23-09-02 11:50:50 Rev 14.05
The Charlesworth Group, Huddersfield 01484 517077

investigated through comparison with both an analytical solution and measurements from a plant trial. Finally, the model has been applied to the specific problem of how the corner radius of the mould affects the thermal, deformation, and stress fields of a low carbon steel billet continuously cast using both oil lubricant and mould powder practices. The implications for longitudinal crack formation are discussed.

PLANT TRIALS

Caster details and nominal operating practice

A plant trial was conducted at POSCO, Pohang works, South Korea, relating to a 120 mm square section of 0·04%C steel continuously cast at 2·2 m min^{-1}. The mould was manufactured from relatively pure, deoxidised high purity (DHP) copper with a wall thickness of 6 mm, a corner radius of 4 mm, and a single 'linear' taper of 0·75%/m. Other operating parameters and mould geometry details are provided in Table 1.

Mould temperature measurement

The mould tube was instrumented with 12 K type thermocouples on the inside radius face as shown in Fig. 2. They were arranged in three columns along the centreline and $\pm$45 mm from the centreline, and in four rows located at 120, 170, 400, and 700 mm below the top of the 800 mm length mould. The thermocouples were embedded in the mould wall to a depth of 3 mm from the hot face. The mould water temperature increase was not recorded at the time, but is estimated to be 30 K based on recent measurements for the same conditions.

Solid shell measurement

To investigate solid shell growth, FeS tracer was suddenly added into the liquid pool during steady state casting. Because FeS cannot penetrate the solid shell, the position of the solid shell front at that instant can be clearly recognised after casting using a sulphur print.

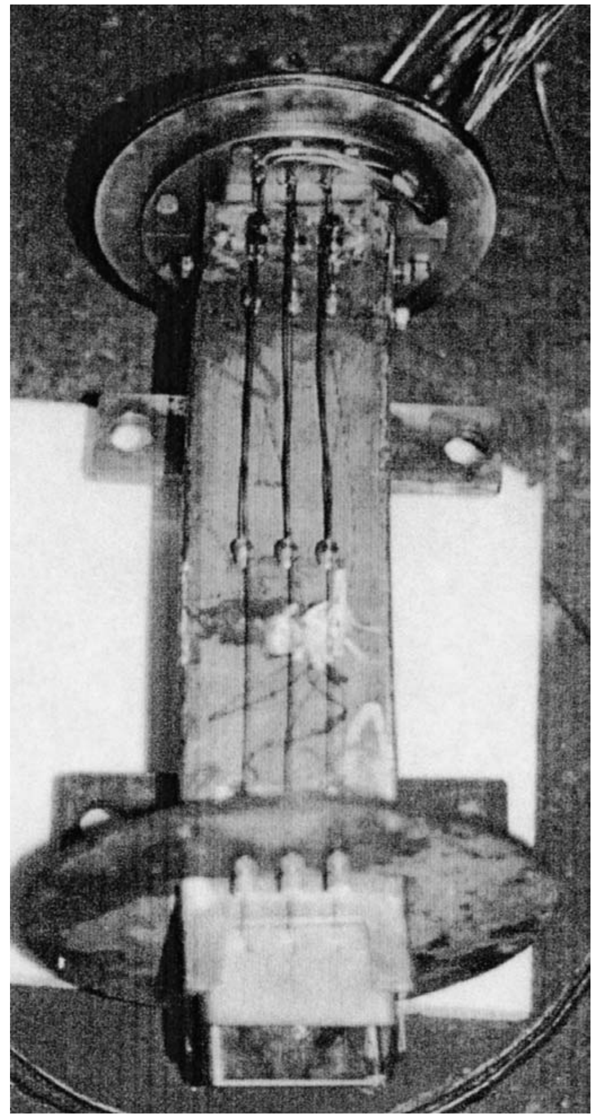

2 Photograph of thermocouple instrumented mould tube

MATHEMATICAL MODEL DESCRIPTION

To investigate the thermomechanical behaviour of the continuous cast billet and mould, a 2D transient thermoelastoviscoplastic finite element model (AMEC2D)[20–22] has been developed. This model tracks the thermal and mechanical behaviour of a transverse slice through the continuously cast strand as it moves down through the caster. The model includes separate finite element models of heat transfer and stress generation that are stepwise coupled through the size and properties of the interfacial gap. Stresses arise primarily as a result of thermal strains, while heat transfer across the gap depends on the amount of shrinkage of the solidifying shell. During each step of the analysis, the temperature fields of the mould and strand are calculated simultaneously, extrapolating from the previous step, neglecting axial conduction. Then, the stress analysis calculates deformation of the strand, stress, and the air gap size. Iteration continues until the heat transfer coefficient determined from the calculated gap is converged.

Table 1 Casting and mould conditions in plant trial

Casting conditions	
billet size	120 mm^2
Nominal casting speed	2·2 m min^{-1}
Meniscus level	100 mm
Oscillation type	Sinusoidal
Stroke length	8 mm
Submerged entry nozzle	Open pouring
Machine radius	8 m
Mould conditions	
Material	Deoxidised high purity Cu
Mould length	800 mm
Thickness	6 mm
Construction	Tube
Taper (linear)	0·75%/m
Corner radius	4 mm
Cooling water	1100 l min^{-1}
Cooling water velocity	9·2 m s^{-1}

Microsegregation analysis

Generally, the solidification of steel during continuous casting does not exactly follow the path of the equilibrium binary Fe–C phase diagram owing to the rapid cooling and microsegregation of other solute elements. To determine the variation of liquid, δ-Fe, and γ-Fe fractions with temperature, the microsegregation of solute elements of steel was analysed using the direct finite difference method of Kim[23] and Ueshima *et al.*[24] as described elsewhere.[25] Figure 3 shows the calculated liquid, δ-Fe, and γ-Fe fractions as a function of temperature during solidification of the low carbon steel grade used in the plant trial (Fe–0·04C–0·2Si–0·25Mn–0·010P–0·015S, wt-%) and the corresponding thermal linear expansion (TLE) function used in the present study. These results were used to determine the thermophysical properties of the steel given below.

ias0001675 23-09-02 11:50:50 Rev 14.05
The Charlesworth Group, Huddersfield 01484 517077

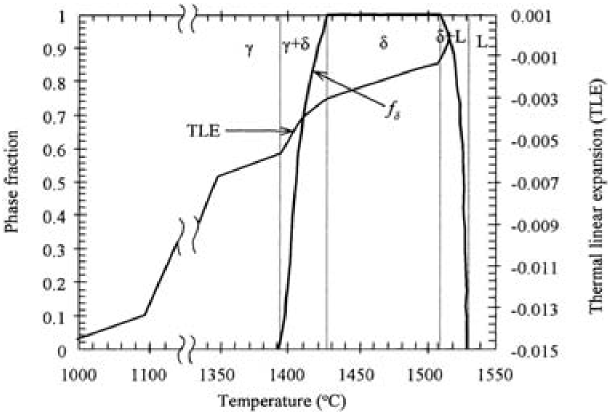

3 Calculated solid fraction f_s, δ-Fe fraction, γ-Fe fraction, and thermal linear expansion as function of temperature for low carbon (C = 0·04 wt-%) steel

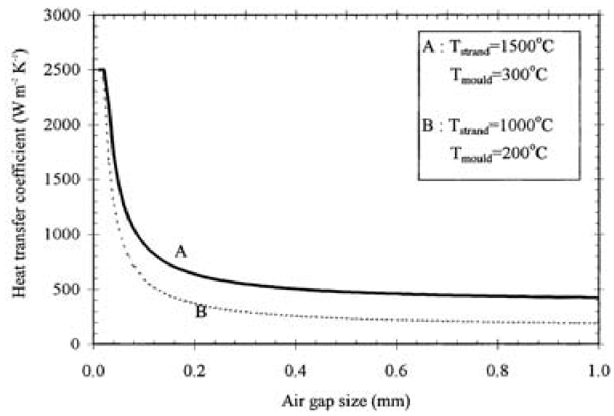

5 Heat transfer coefficient across strand/mould for various air gap sizes and given surface temperatures

Heat flow analysis

The heat flow model solves the 2D transient heat conduction equation for the temperature distribution in the solidifying shell. The effects of solidification and solid state phase transformation on the heat flow are incorporated through a temperature dependent enthalpy function as shown in Fig. 4. This figure also shows the temperature dependent conductivity function.

The following assumptions are used in this calculation:

(i) the incoming metal temperature, liquid level, and casting speed are constant and axial heat conduction is ignored

(ii) mould oscillation and friction between the shell and the mould are neglected

(iii) the effect of convective heat flow in the liquid region is taken into account using the effective thermal conductivity k_{eff} for molten steel[26]

$$k_{\text{eff}} = 27[1 + 6(1 - f_s)^2] \quad (1)$$

where f_s is the solid fraction.

Oil casting interface heat transfer

Heat extraction from the solid shell surface in the mould is primarily controlled by heat conduction across the interface between the mould and the solidifying steel shell. This is modelled as an internal boundary condition, using the interfacial heat transfer coefficient h_C as a function of air gap thickness and surface temperature of the strand, according to the relationship of Kelly *et al.*[10]

$$h_C = h_{\text{rad}} + \frac{1}{R_T} = h_{\text{rad}} + K_g/d_{\text{gap}} \quad (2)$$

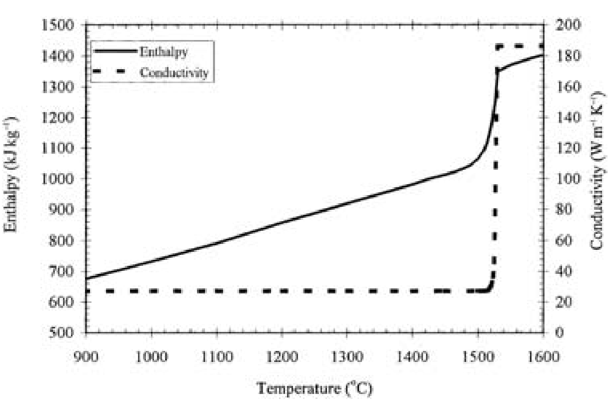

4 Enthalpy and conductivity of low carbon steel (C = 0·04 wt-%) used in present model

where R_T is the thermal resistance, K_g is the thermal conductivity of the gap medium (assumed to be 100% air in the present study), given in Table 2, d_{gap} is the thickness of the gap, and h_{rad} is the heat transfer coefficient for radiative heat flow when an air gap exists between the strand and the mould such that

$$h_{\text{rad}} = \sigma_{\text{SB}}\varepsilon(T_s + T_m)(T_s^2 + T_m^2) \quad (3)$$

where σ_{SB} is the Stefan–Boltzmann constant, T_s is the shell surface temperature, and T_m is the mould hot face temperature. The average emissivity ε of the shell and mould surface is assumed to be 0·8.[27] If the value of h_C computed from equation (2) exceeds the value associated with direct contact, it is truncated to that value. The value of h_C for direct contact is taken to be 2500 W m^{-2} K^{-1}, which represents a minimum contact resistance or average gap associated with oscillation marks of 0·02 mm depth.[10] Figure 5 shows plots of this heat transfer coefficient function versus air gap size, assuming strand surface temperatures of 1500 and 1000°C and mould hot face temperatures of 300 and 200°C.

Powder casting interface heat transfer

To study the effect of using mould powder as a lubricant, simulations were also performed using the following expression for thermal resistance between the solidifying shell surface and the mould, consisting of four terms

$$R_T = \frac{1}{h_m} + \frac{d_{\text{gap}}}{K_g} + \frac{d_{\text{flux}}}{K_{\text{flux}}} + \frac{1}{h_{\text{shell}}} \quad (4)$$

The first thermal resistance (first term in equation (4)) is the contact resistance between the mould wall surface and the mould flux, where h_m is the contact heat transfer coefficient set to 2500 W m^{-2} K^{-1}. The second resistance is conduction through the air gap, which is the same as calculated for oil casting. The third resistance is conduction through the mould flux film, with a thermal conductivity K_{flux} of 1·0 W m^{-1} K^{-1}.[21] The thickness of the mould flux layer d_{flux} is assumed to be 0·1 mm.[28] The final term is the contact resistance between the mould flux and the strand surface, where the heat transfer coefficient h_{shell} depends

Table 2 Conductivity of gap medium (air) with temperature

Temperature, °C	Conductivity, W m^{-1} K^{-1}
200	0·032
400	0·039
600	0·045
800	0·051
1000	0·057
1200	0·063
1400	0·068

ias0001675 23-09-02 11:50:50 Rev 14.05
The Charlesworth Group, Huddersfield 01484 517077

greatly on temperature, because of the large change in viscosity of the mould flux over the temperature range of the strand surface. The temperature dependency of h_{shell} is given in Table 3.[29]

Spray cooling

To investigate bulging of the billet below the mould, thermal calculations were extended to 200 mm below the mould exit, assuming a value of 500 W m^{-2} K^{-1} for the heat transfer coefficient at the billet surface and ambient temperature of 30°C. This value was chosen to represent a typical spray cooling coefficient, which ranges from 200 to 600 W m^{-2} K^{-1} in the literature.[30]

Mould temperature

Temperature in the mould was assumed to be steady within each time step and slice. It was calculated in AMEC2D by applying the water heat transfer coefficient to the cold face of the mould based on the correlation of Dittus and Boelter.[31] This analysis ignores axial heat conduction. Thus, a second model, CON1D,[32] was applied to validate the heat flux profile. This model takes into account axial heat conduction in the mould, so gives more accurate mould temperature predictions than AMEC2D.

Stress analysis

The stress and strain distributions associated with temperature change in the transverse slice of the solidifying shell are calculated by the solving the standard equilibrium, stress–strain, and small strain displacement equations. The slice is assumed to be in a plane strain condition, in which strain along the casting direction is neglected. The temperatures calculated by the thermal model are input to the incremental thermal stress model.

Mould taper and distortion

Mould distortion due to thermal expansion, which is added to the mould taper to define the mould wall position, is calculated from

$$\Delta x_{\text{mould}} = \alpha_{\text{mould}} \left(\frac{\text{mould width}}{2} \right) \left(\frac{T_{\text{cold}} + T_{\text{hotc}}}{2} - T_{\text{ref}} \right) \quad (5)$$

where α_{mould} is the mould thermal linear expansion coefficient ($1{\cdot}6 \times 10^{-5}$ K^{-1}), T_{cold} is the mould cold face temperature (°C), T_{hotc} is the mould hot face temperature (°C), and T_{ref} is the average mould temperature at the meniscus (°C).

For equation (5), the mould temperature is based on the results of the CON1D model,[33] which matches well with the measured temperature. Figure 6 shows profiles of the mould distortion, 0·75%/m linear profile of the mould taper, and the actual mould wall shape adopted in the present work as the wall boundary condition.

Thermal strain

Thermal strain arises from the volume changes caused by changing temperature and phase transformation. This was calculated from the temperature determined in the heat transfer analysis and the thermal linear expansion of steel (TLE), which can be determined in turn from the phase fractions found by microsegregation analysis and the specific volume V of each phase of the steel

$$\text{TLE}(T) = \left(\frac{V}{V_{\text{ref}}} - 1 \right)^{1/3} \quad (6)$$

$$V = (f_\delta V_\delta + f_\gamma V_\gamma) f_s + V_l f_l \quad (7)$$

where V_{ref} is the specific volume at the reference temperature, and f_δ, f_γ, and f_l are fractions of δ, γ, and liquid phase, respectively. The reference temperature is chosen to correspond with the solid fraction of 0·8. The specific volume of the various phases is given in Table 4, and were obtained from Wray.[34]

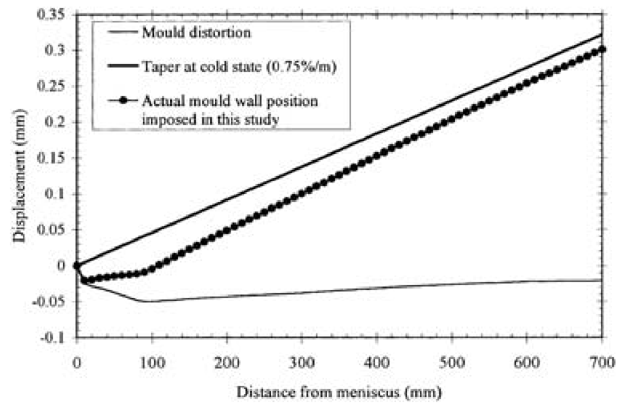

6 Profiles of mould distortion and taper used in present model

Effective plastic strain and flow stress in carbon steel

At higher temperatures, important to stress development during solidification, inelastic strain from plasticity and creep is also important. The following constitutive equation proposed by Han and co-workers[35–37] is used to relate the flow stress of δ and γ phases at various temperatures T and strain rates $\dot{\varepsilon}_p$

$$\dot{\varepsilon}_p = A \exp(-Q/RT)[\sinh(\beta K)]^{1/m} \quad (8)$$

$$\sigma = K \varepsilon_p^n \quad (9)$$

where A and β are constants, Q and R are the activation energy for deformation and the gas constant, respectively, m is the strain rate sensitivity, K is the strength coefficient, n is the strain hardening exponent, σ is the flow stress, and ε_p is the effective plastic strain. Table 5 gives the parameters in the above equation for δ ferrite and γ austenite phases of steel. The total strain rate is thus composed of this viscoplastic strain rate together with the thermal and elastic strain rates.

Table 3 Temperature dependence of heat transfer coefficient between mould flux and strand surface[29]

Temperature, °C	h_{shell}, W m^{-2} K^{-1}
Mould flux crystalline temperature, 1030°C	1000
Mould flux softening temperature, 1150°C	2000
Metal solidus temperature, 1511°C	10 000
Metal liquidus temperature, 1529°C	20 000

Table 4 Specific volume of δ-Fe, γ-Fe, and liquid steel[34]

Phase	Specific volume, cm^3 g^{-1}
δ	$0{\cdot}1234 + [9{\cdot}38 \times 10^{-6}(T-20)]$
γ	$0{\cdot}1255 + [9{\cdot}45 \times 10^{-6}(T-20)] + (7{\cdot}688 \times 10^{-6})$
Liquid steel	1/7·035

Table 5 Parameters for constitutive equation[37]

Phase	A, s^{-1}	β, MPa^{-1}	Q, kJ mol^{-1}	m	n
δ	$6{\cdot}754 \times 10^{8}$	0·0933	216·9	0·1028	0·0379
γ	$1{\cdot}192 \times 10^{10}$	0·0381	373·4	0·2363	0·2100

ias0001675 23-09-02 11:50:50 Rev 14.05
The Charlesworth Group, Huddersfield 01484 517077

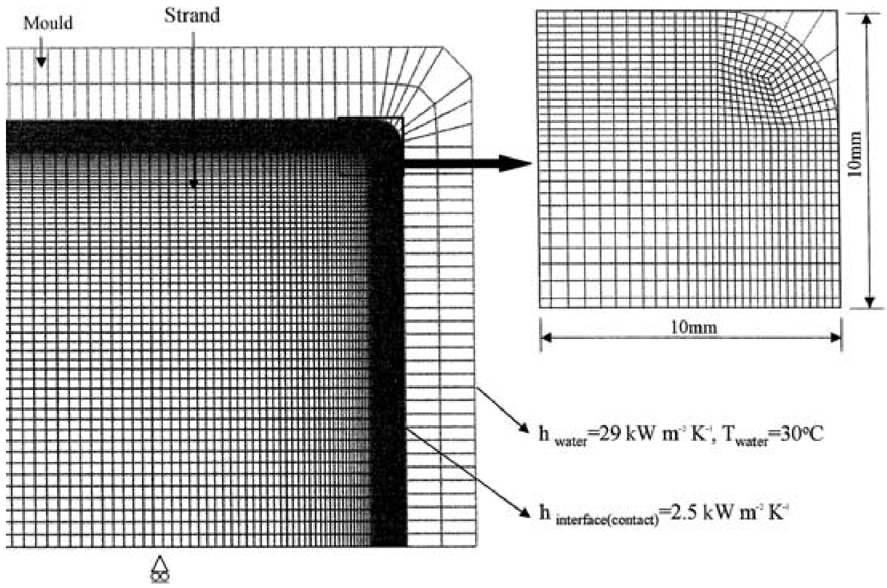

7 Finite element mesh of two-dimensional horizontal quarter domain for billet strand and mould and its boundary conditions: *h* heat transfer coefficient, *T* temperature

Elastic modulus

The elastic modulus of steel decreases significantly with increasing temperature. There is still uncertainty concerning the best value of E at high temperatures. The following expression of Kinoshita *et al.*[38] is used in the present work

$$E = 1{\cdot}38 \times 10^{-2}\,T^2 - 225{\cdot}6T + 3{\cdot}146 \times 10^5\ (\mathrm{kg\ cm^{-2}}) \qquad (10)$$

Treatment of liquid

Since elements may be liquid, solid, or mushy, and the volume of liquid in the domain may vary, special care is needed to handle the liquid region. In the present model, negligible ($0{\cdot}5 \times 10^{-4}$ MPa) stiffness is assigned to those Gaussian integration points whose temperature is above the coherence temperature, assumed to correspond to a solid fraction of 0·7. In addition, thermal expansion is assumed to be zero for temperatures corresponding to a solid fraction of 0·8 or above.

Solid shell–mould contact

Interaction between the shell and the mould affects not only the loading on the exterior position of the shell, but also influences the heat transfer significantly. A contact algorithm is applied to restrain the shell elements from penetrating the mould,[39] whose position is defined in Fig. 6. At each iteration, such penetrations are evaluated, a new global matrix is generated, and stresses are resolved. To achieve convergence, the penetration parameter is set to 5·0, and the friction coefficient to 0·2.

Ferrostatic pressure and bulging

Ferrostatic pressure from the vertical gravity force on the liquid pushes the inside surface of the solidifying shell towards the mould walls, and greatly affects gap size and mould heat transfer. It increases in proportion to the distance below the meniscus. In AMEC2D, this pressure is applied to every liquid element in the domain at all times. This pressure is allowed to cause bulging below the mould simply by removing the mould contact constraint conditions. This approach neglects the effects of axial bending moments and guide rolls, so represents an extreme case of poor guide roll alignment.

Crack criterion

To study the susceptibility of corner crack occurrence, 'hoop stress' σ_h and 'hoop strain' ε_h components were calculated to show the transverse stress–strain component oriented parallel to the perimeter of the shell. To calculate these hoop values, first, the angle of the heat flux direction ϕ with respect to the global x and y axes is obtained from the temperature results. The stress–strain component perpendicular to that direction, i.e. $\theta = 90° - \phi$, is then derived from

$$\sigma_h = \frac{\sigma_x + \sigma_y}{2} + \frac{\sigma_x - \sigma_y}{2}\cos 2\theta + \tau_{xy}\sin 2\theta \qquad (11)$$

where σ_x is the x stress, σ_y is the y stress, and τ_{xy} is the shear stress.

Note that along the horizontal shell, $\theta = 0°$, so the hoop stress becomes σ_x. The hoop stress becomes σ_y along the vertical shell, as $\theta = 90°$. Similar calculations are applied to find the hoop strain ε_h.

Strand and mould domain

Figure 7 shows the finite element mesh of the 2D horizontal section of the billet strand and mould and its boundary conditions. A twofold symmetry assumption allows a quarter transverse section of the billet to be modelled. This domain consists of 5273 nodes and 5135 four node isoparametric quadrilateral elements in the billet, and 207 nodes and 136 elements in the mould for the 4 mm radius mould. For the 15 mm radius mould, the finite element mesh contains 8947 nodes and 8775 elements in the billet, and 243 nodes and 160 elements in the mould. The element equations are assembled using a single integration point, and the equations are solved using Newton–Raphson iteration. Further model details are given elsewhere.[39] The boundary conditions used are also shown in Fig. 7. Further simulation conditions for the plant trial are described in Table 6.

Table 6 Simulation conditions for plant trial

Steel grade	C = 0·04 wt-%
Liquidus temperature[40]	1529°C
Solidus temperature[40]	1511°C
Superheat	25 K
Contact heat transfer coefficient	2500 W m^{-2} K^{-1}
Mould–water heat transfer coefficient	29 400 W m^{-2} K^{-1}
Casting speed	2·2 m min^{-1}
Taper	0·75%/m

ias0001675 23-09-02 11:50:50 Rev 14.05
The Charlesworth Group, Huddersfield 01484 517077

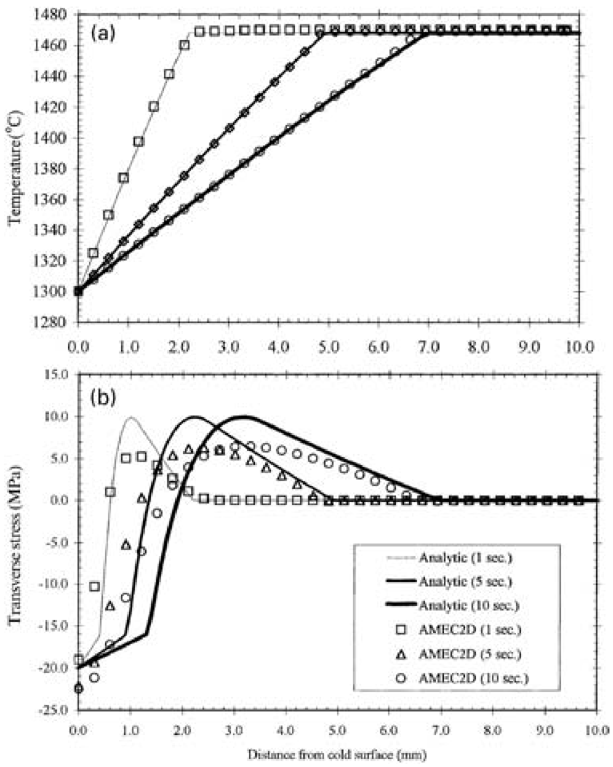

a temperature; *b* stress

8 Comparison of numerical and analytical solutions

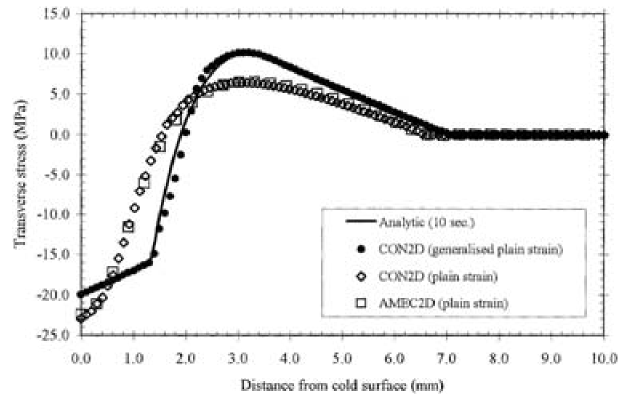

9 Comparison of calculated stress profiles with analytical solutions

MODEL VALIDATION

Comparison with analytical solution

The internal consistency of the finite element model developed in the present work (AMEC2D) has been validated with analytical solutions under the condition of plane strain using an element mesh size of 0·3 mm, as shown in Fig. 7. Weiner and Boley[41] developed an exact analytical solution of thermal stress during one-dimensional solidification of a semi-infinite elastic–perfectly plastic body after a sudden decrease in surface temperature. Table 7 gives the detailed conditions for verification of the analytical solution.

Figure 8 compares this solution with numerical calculations for various solidification times. Although the temperature profile of AMEC2D agrees closely with the analytical solution (Fig. 8*a*), the maximum tensile and compressive stresses are 6·5 MPa and −22·9 MPa, which differ from the analytical solution by 34% and 11·5%, respectively (Fig. 8*b*). This discrepancy is caused by the assumption of plane strain in AMEC2D, which is different from the true state of generalised plane strain in the analytical solution. However, comparing AMEC2D results with those of the CON2D model[42,43] using a fine mesh size of 0·1 mm, as seen in Fig. 9, both show almost the same stress profile, which implies that the mesh size adopted in the present work is adequate.

Table 7 Simulation conditions for analytical solution test[41]

Density	7400 kg m^{-3}
Specific heat	700 J kg^{-1} K^{-1}
Thermal conductivity	33 W m^{-1} K^{-1}
Latent heat	272 kJ kg^{-1}
Initial temperature	1469°C
Liquidus temperature	1469°C
Solidus temperature	1468°C
Surface temperature	1300°C
Young's modulus	40 GPa
Poisson's ratio	0·35
Thermal expansion coefficient	20×10^{-6} K^{-1}
Yield stress at surface temperature	20 MPa

Comparison with plant trial

The 2D transverse slice model for simulating billet casting under the plane strain condition described above was validated by comparing with measurements from the plant trial, based on the conditions given in Table 6, featuring oil casting with a 4 mm corner radius.

Temperature

Axial mould–temperature profiles were calculated using both the AMEC2D and CON1D models. Figure 10 compares the predictions with the measured temperature profile down the mould, found by averaging the thermocouple values across each of the four rows. The heat flux profile in the CON1D model was adjusted carefully, to match the temperatures accurately. The AMEC2D model ignores axial heat conduction so is not expected to match exactly, but still agrees reasonably well. Figure 10 also includes the hot and cold face temperatures.

The corresponding heat flux profiles predicted by both models are compared in Fig. 11. The accurate CON1D model curve shows a slight dip and rebound in heat flux between ~20 and 100 mm below the meniscus. This is a result of the unexpected lower temperature measured by the highest thermocouple. It is interesting to note that this drop corresponds approximately to the region of negative mould distortion, suggesting that this negative taper at the meniscus might play a role. This heat flux dip phenomenon has been observed by others.[13,44,45] The AMEC2D curve shows the classic monotonically decreasing profile, which is more commonly observed.

The heat flux for the mould powder casting case is also included in Fig. 11. Its overall profile is much lower than that for the oil casting case. This result also agrees

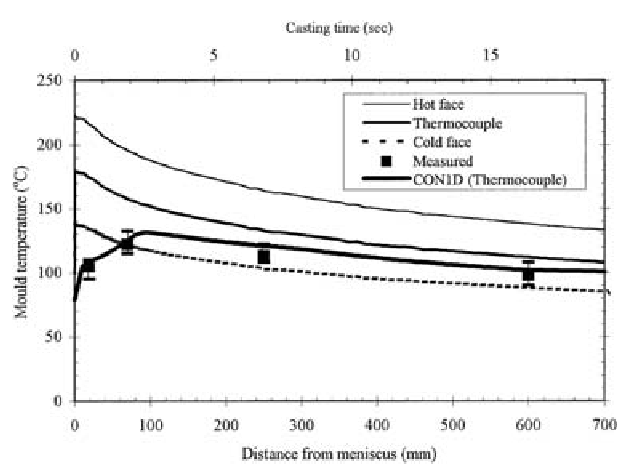

10 Comparison of measured and calculated mould temperatures

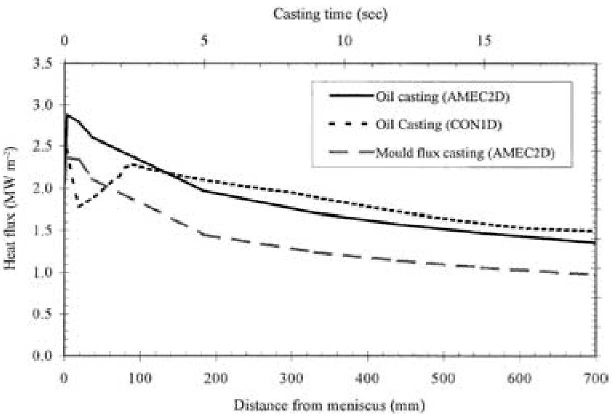

11 Heat flux profiles down mould for given casting conditions and models

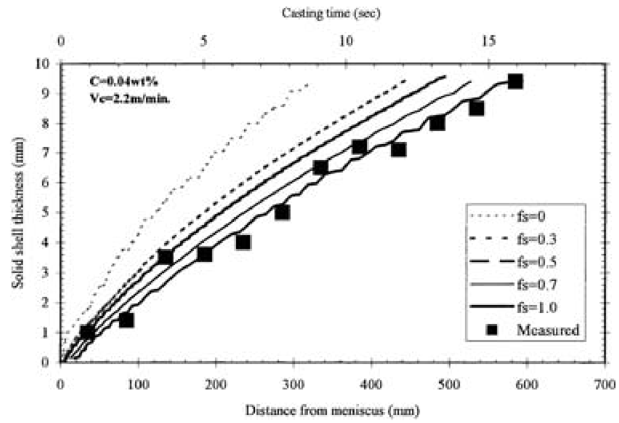

13 Comparison of measured and calculated solid shell thicknesses with casting time: V_c casting speed

with other work.[46] This lower heat flux is caused by the insulating effect of the mould flux layer between the mould and strand.

Heat balance

To validate the heat flux profiles, a comparison was made with an energy balance carried out for the cooling water. The model predictions of average heat flux, found from the areas under the curves in Fig. 11, are 1·84 and 1·80 MW m^{-2} for CON1D and AMEC2D, respectively. The measured cooling water temperature increase of 8 K corresponds to an average heat flux of 1·84 MW m^{-2}, which agrees well with both model predictions.

Solid shell thickness

Figure 12 compares the measured solid shell thickness in a transverse section through the billet with the corresponding model prediction. The transverse section was taken at 285 mm below the meniscus, which corresponds to a simulation time of 7·8 s. The deformed shape of the strand is superimposed with temperature contours in Fig. 12. Shell thickness is defined in the model as the isotherm corresponding to the coherency temperature, assumed to be 70% solid. The general shapes of the predicted and measured solid shell match reasonably. It is noted that the model can also predict the re-entrant corner effect, observed in the sulphur print. This agreement appears to validate the remaining features of the present model, including air gap formation in the corner region.

The shell thickness is plotted in Fig. 13 as a function of residence time in the mould. Also plotted in Fig. 13 are the plant trial measurements, by means of the tracer test. It can be seen in Fig. 13 that the predicted solid shell growth is reasonable, considering the uncertainty about the penetration depth of the tracer into the mushy zone of the solidifying shell.

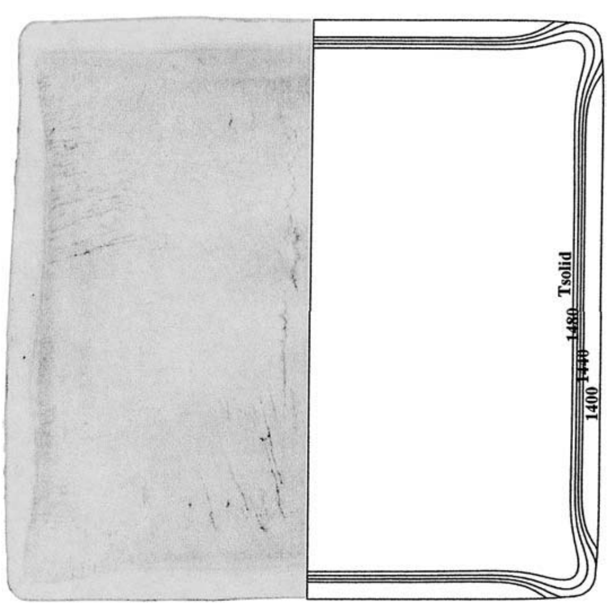

12 Comparison of calculated and measured solid shell thicknesses: C = 0·04 wt-%, 285 mm below meniscus, casting speed 2·2 m min^{-1}

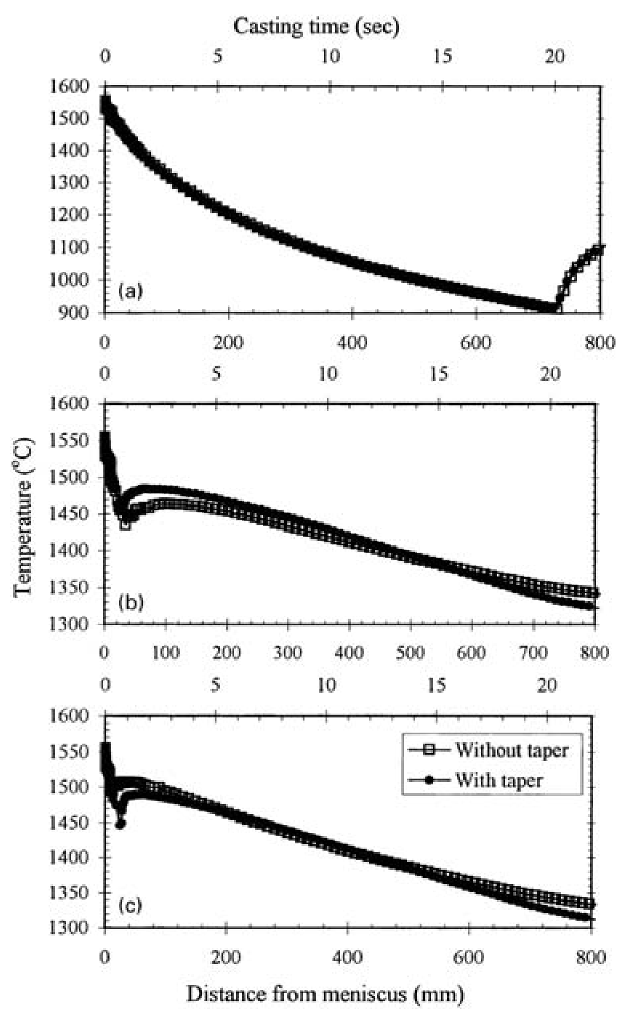

a centre; *b* off corner; *c* corner

14 Evolution of surface temperature profiles at given billet positions for 4 mm corner radius

ias0001675 23-09-02 11:50:50 Rev 14.05
The Charlesworth Group, Huddersfield 01484 517077

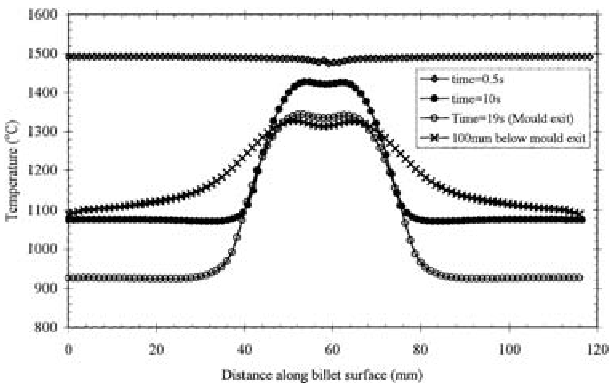

15 Surface temperature profiles along 4 mm corner radius billet at given times

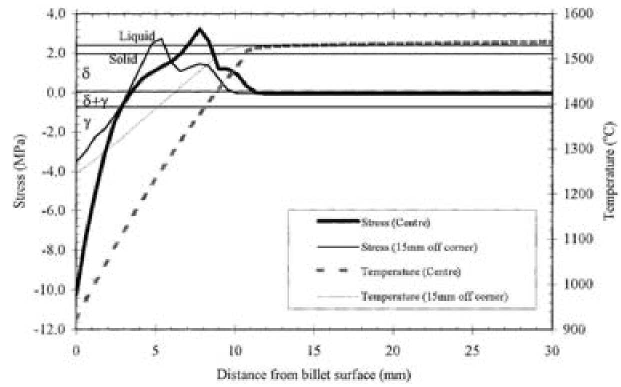

17 Temperature and transverse stress profiles through shell thickness at 19 s of casting time for 4 mm corner radius mould

Bulging below mould

Bulging below the mould depends on the temperature and strength of the shell at the mould exit. In the mould, the surface temperature of the strand is governed by the contact between the strand and the mould, which defines the gap between them. This is influenced by the mould taper, so a simulation was also done for the extreme case of no mould taper. Figure 14 shows axial profiles of the surface temperature at the strand centre, corner, and 5 mm off corner. Regardless of taper, the centreline surface temperature has the same profile, decreasing monotonically to 900°C at the mould exit (Fig. 14*a*). This is because the billet strand is always in good contact with the mould at the strand centre. The temperature rebound below the mould is simply due to the slower rate of heat removal by the sprays.

At the corner region, the temperature rebounds after ~1 s for both cases, owing to air gap formation. This time corresponds to initial formation of the air gap, and is delayed by applying the taper, as shown in Fig. 14*c*. An air gap still forms, because the taper of 0·75%/m is not sufficient to match the shrinkage of the shell. Figure 15 depicts transverse temperature profiles along the billet surface at various casting times, with taper. After the initial solidification stage (0·5 s), the temperature around the corner region is shown to remain higher throughout casting. This was not observed by Brimacombe *et al.*,[3] who did not simulate air gap formation during the calculation. They attributed off corner internal cracks to a hinging action around a cold, strong corner. However, Fig. 15 implies that the corner region has a higher surface temperature, which enhances hinging below the mould.

The strand shell exiting the mould is weak and hot, so the internal liquid pressure bulges the shell outwards below the mould. Although it might be supposed that this bulging in billet casting is small, compared with slab casting, the higher casting speeds and lack of support can make it significant. This bulging can cause internal strain in the shell, depending on billet geometry features such as corner radius and taper. Figure 16 shows the evolution of displacement at the centre and corner of the billet surface. As seen in Fig. 16, the bulging at the centre of the billet is predicted to be ~1·4 mm for 4 mm corner radius of billet with

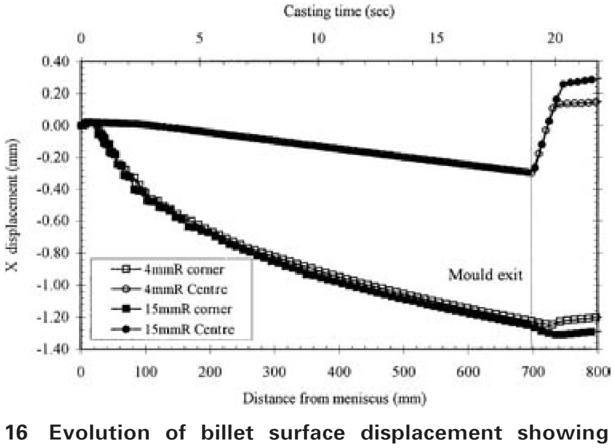

16 Evolution of billet surface displacement showing bulging below mould exit with given corner radii *R*

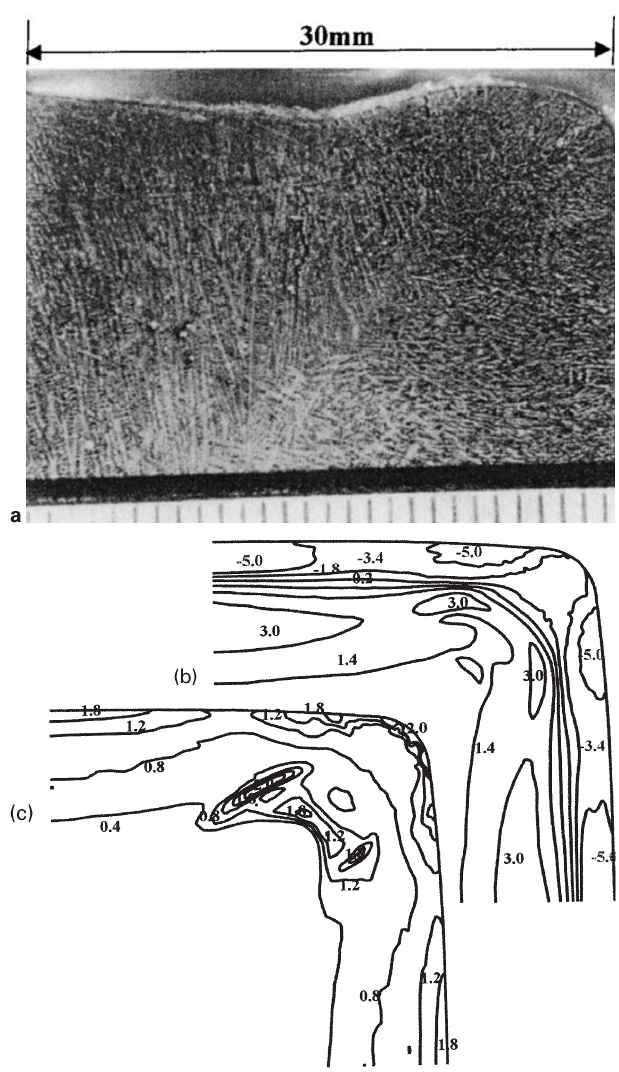

a microstructure of off corner crack; *b* hoop stress distribution; *c* equivalent plastic strain contours

18 Comparison of crack location and model calculations at 100 mm below mould exit

ias0001675 23-09-02 11:50:50 Rev 14.05
The Charlesworth Group, Huddersfield 01484 517077

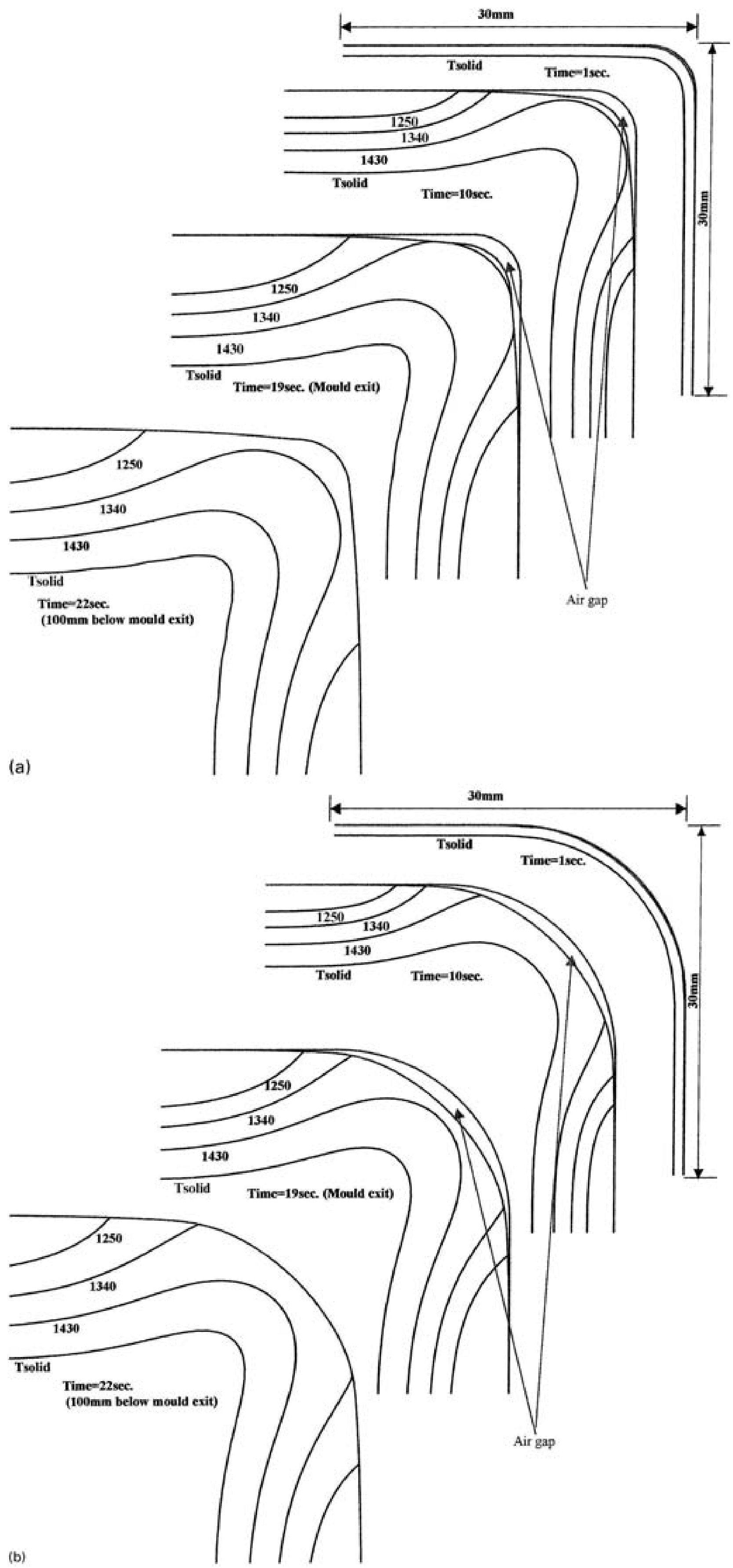

a 4 mm corner radius; *b* 15 mm corner radius

19 Variation of shell profiles and temperature contours in corner region

ias0001675 23-09-02 11:50:50 Rev 14.05
The Charlesworth Group, Huddersfield 01484 517077

respect to displacement of the billet corner. Bulging of the billet during the plant trial was also measured, based on the distance from the billet centre to the non-bulged line extending between the two billet off corner locations (4 mm from each edge). These measurements were made on the cold section, and ranged greatly from 0 to over 2 mm. Considering the uncertainties when evaluating the bulging, the calculated bulging amount seems to be consistent with the measured value.

Stress and crack prediction

To illustrate the stress state through the solidifying shell, transverse stresses σ_x are plotted at various strand positions at 19 s of casting time (mould exit) in Fig. 17. The peak tensile stress is $\sim$3 MPa, and is found beneath the surface. In the mould, it is similar around the billet perimeter except near the corner. The peak compressive stress is found at the surface, and is much higher at the centre region than at the off corner and corner. This is because of the huge drop of surface temperature, resulting from good contact between the strand and the mould, which increases the shell strength. The superimposed temperatures (Fig. 17) through the shell show that the peak stress clearly corresponds to the δ ferrite region, as indicated by the horizontal lines. This agrees with the findings of Moitra *et al.*,[43] that the sudden shrinkage from the δ to the γ phase produces these tensile peaks, which may cause subsurface cracks.

During the plant trial, billet samples were also taken under the same casting conditions as described in Table 1, and their microstructure was investigated. Figure 18 compares the typical microstructure of an off corner crack that was found in this plant trial with stress and strain development at 100 mm below the mould exit. Usually, solidification cracking or hot tearing can occur when the steel in the mushy zone is under tension beyond some small critical limit, owing to the existence of a liquid film. Peak hoop tensile stresses, which pull apart dendrites and result in hot tears, take place both at the centre and at the off corner of the billet, as shown in Fig. 18*b*. Effective plastic strain is highest at the off corner location (Fig. 18*c*). It is interesting to note that the peak strain occurs in a region of tensile hoop stress, and corresponds roughly to the position of crack occurrence. The exact location of this crack obviously matches the surface depression.

EFFECT OF MOULD CORNER RADIUS

Next, the model was applied to compare the thermomechanical behaviours of steel cast in 4 mm (small) and 15 mm (large) corner radius moulds. The results have been evaluated according to the effects on heat transfer and gap formation, longitudinal corner surface cracks, and longitudinal off corner subsurface cracks.

Heat transfer

Figure 19 shows temperature contours with the deformed shapes of both billets near the corner region, at four locations down the mould. Both billets experience increasing solid shell thinning at the corner, and the associated evolution of an air gap, with increasing casting time. During initial solidification, a uniform solidifying shell forms as a result of good contact between the strand and mould. After less than 1 s, the shell starts to shrink away from the billet and an air gap forms near the corner. This reduces the local heat flow from the strand to the mould. This raises the temperature of the corner regions 22 mm below the meniscus, as shown in Fig. 14. Closer examination of the temperature profile around the corner reveals that the 15 mm corner radius billet develops both higher surface temperature at the corner and more severe non-uniform temperature contours along the billet surface as solidification proceeds. This re-entrant corner effect persists even below the mould exit.

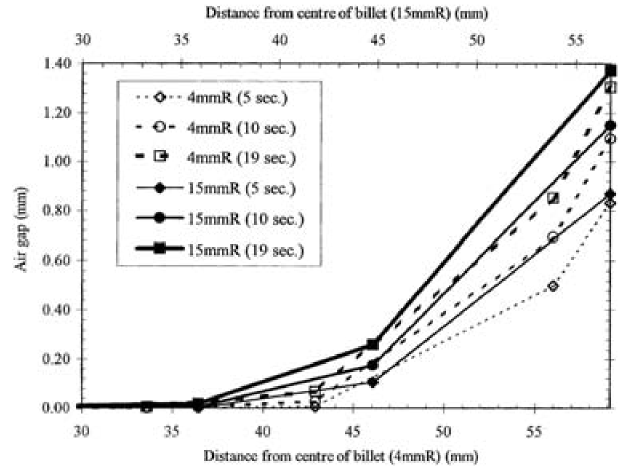

20 Evolution of air gap size profiles with given corner radii

The air gap size for both moulds is plotted at various casting times in Fig. 20. As time progresses, with increasing distance below the meniscus, the gap spreads further around the corner. By the mould exit, the gap size extends to $\sim$1·3 mm around the corner of the 4 mm radius billet and 1·4 mm for the 15 mm radius billet. In fact, the gap size in the 15 mm radius mould is larger than that of the 4 mm radius mould at every time. This leads to a higher surface temperature, as shown in Fig. 19. The air gap grows with thermal contraction of the circumference of the long, thin shell. The circumferential length along the billet surface is 118·3 mm and 113·6 mm for the 4 mm and 15 mm radius mould, respectively. Shell shrinkage is 2·38 mm for the 4 mm and 1·95 mm for the 15 mm radius billet. The 15 mm radius billet shrinks a little less because its shell is slightly hotter. However, the present study shows that the 4 mm corner radius is associated with a smaller air gap size. This result is opposite to that of Ohnaka and Yashima,[19] who simulated slab casting and reported that the air gap size decreased with increasing corner radius, resulting in lower stress near the corner.

The larger air gap size predicted for the large corner radius in the present work is consistent with the simple analysis of the strand geometry described in the Appendix. For a given amount of shrinkage, the shell perimeter around the large radius corner must pull further away from the wall than in the small radius case, which generates 'slack' more easily. This larger air gap can also be guessed from the extreme case of large corner radius: a round section billet, where an air gap tends to form around the entire perimeter.

Longitudinal corner surface cracks

Figure 21 compares contours of hoop stress and hoop plastic strain of both billets near the corner region at the casting time of 8 s. As can be seen in Fig. 21, both hoop values are much higher in the 15 mm radius billet. The development of hoop plastic strain with time is shown in Fig. 22 at a critical corner location, 1 mm beneath the corner surface, where longitudinal corner cracks were found. Figure 22 reveals that the large corner radius billet develops tensile plastic strain from 4 to 14 s in the mould (150–520 mm below the meniscus). This is consistent with breakout shell observations, in which corner cracks begin some distance below the meniscus. Compression is found both before and after this time. Below the mould, bulging causes the shell to hinge around the corner, forcing the corner surface into compression. The small radius billet experiences compressive plastic strain at this location throughout casting, owing to two-dimensional cooling at

ias0001675 23-09-02 11:50:50 Rev 14.05
The Charlesworth Group, Huddersfield 01484 517077

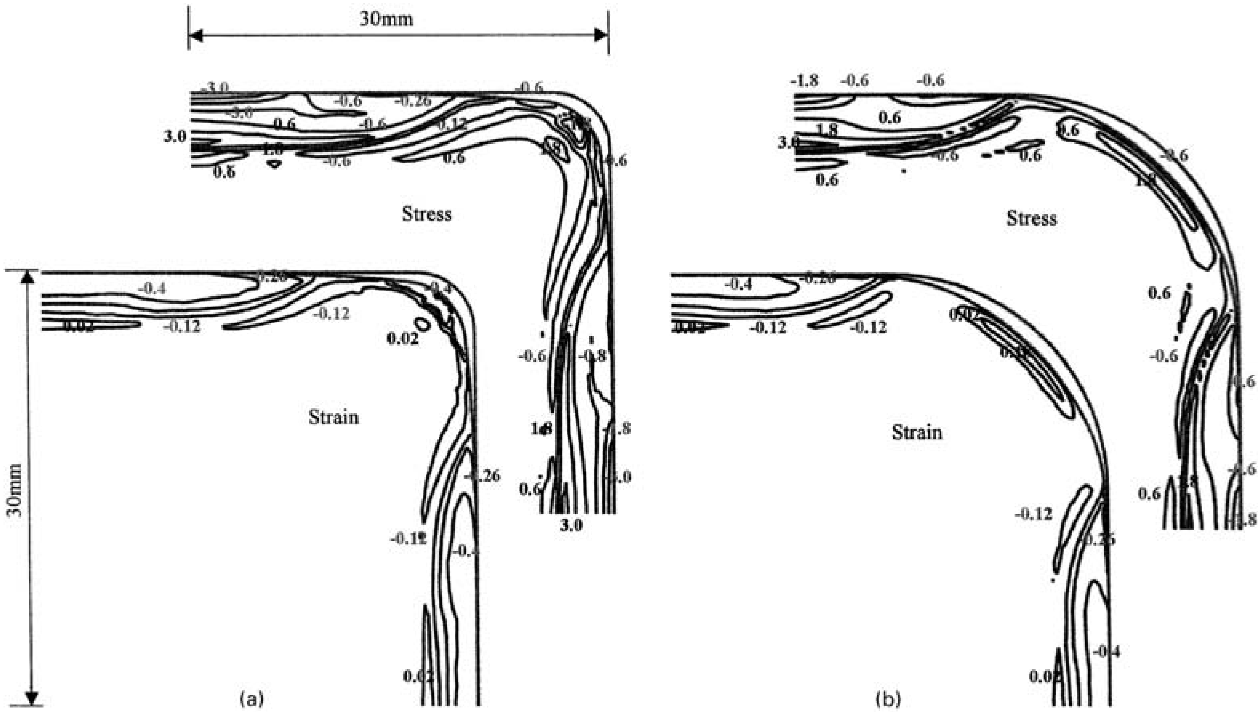

a 4 mm corner radius; *b* 15 mm corner radius

21 Contours of hoop stress and hoop plastic strain at 8 s of casting time for oil casting

the corner. This finding of higher susceptibility to surface cracks with a larger corner radius corresponds well with other plant observations.[1–2] It is also noted from Fig. 22 that using the mould powder as a lubricant can reduce the plastic strain owing to the formation of a more uniform shell, resulting in less crack occurrence.

Longitudinal off corner internal cracks

Figures 23 and 24 compare contours of hoop stress and hoop plastic strain of both billets near the corner region at the mould exit and 100 mm below the mould. All results indicate compression at the surface, which implies that no surface cracks can form at the mould exit or below. Both billets develop similar maximum tensile hoop stresses of ~ 3 MPa, located close to the solidification front everywhere except near the corner. Although the stress changes little between mould and below, the hoop plastic strain changes dramatically. At 100 mm below the mould, bulging of the billet causes the face to hinge around the corner. This causes subsurface tensile strain, increasing from a peak of only 0–0·1% at mould exit to over 0·4% at 100 mm for both billets. The location of the peak strain also moves from the corner to off corner with decreasing corner radius. This movement of the peak strain location is directly related to the shell behaviour at the corner. The shell is thicker at the corner than at the off corner for the small radius billet, while the shell in the large radius billet is thinnest, hottest, and weakest at the exact centre of the corner. Therefore, the small radius billet is more susceptible to off corner subsurface cracks than the large radius billet, as suggested by Samarasekera and Brimacombe.[12] Furthermore, the high peak strain beneath the corner of the large radius billet below the mould suggests that surface corner cracks, which initiate easily in the mould as indicated above, may grow more severe below the mould, as shown in Fig. 1*a*.

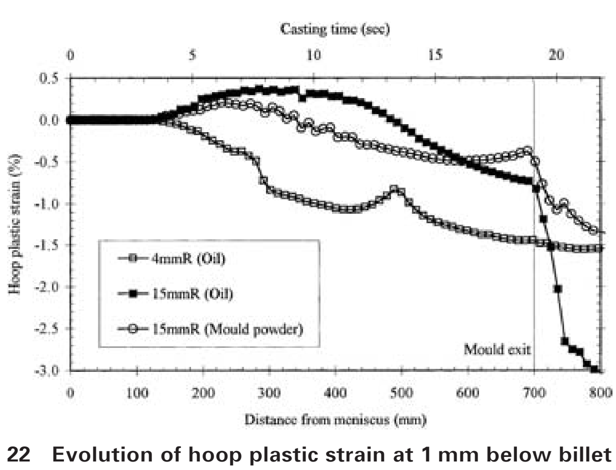

22 Evolution of hoop plastic strain at 1 mm below billet corner surface for given casting conditions

EFFECT OF CASTING WITH MOULD FLUX

Finally, a simulation was carried out to study the effect of mould powder lubrication on the thermomechanical behaviour of steel cast in the two different corner radius moulds but with the same inadequate linear taper. Figure 25 compares the solid shell contours at the mould exit. Both billets show more uniform shell solidification with mould flux, leading to a smaller air gap size, despite having a thinner average shell owing to the lower heat flux associated with a thicker gap. The smaller air gap size is a result of less shrinkage of the hotter shell. In oil casting, this extra uniformity could be achieved by increasing the taper.

Changing the lubricant from oil to powder does not change the nature of the stress and strain development, or the susceptibility of large and small corner radius billets to corner and off corner cracks, respectively. The 15 mm corner radius billet develops peak hoop stress and strain at the corner and the 4 mm corner radius billet generates both peaks at the off corner region. Figure 26 shows the evolution of hoop stress and strain with casting time for the 15 mm corner radius billet. With powder, the heat flux is lower and the solidifying shell is hotter and weaker. Thus, all of the stresses and strains, and the associated surface defects, are exacerbated slightly.

ias0001675 23-09-02 11:50:50 Rev 14.05
The Charlesworth Group, Huddersfield 01484 517077

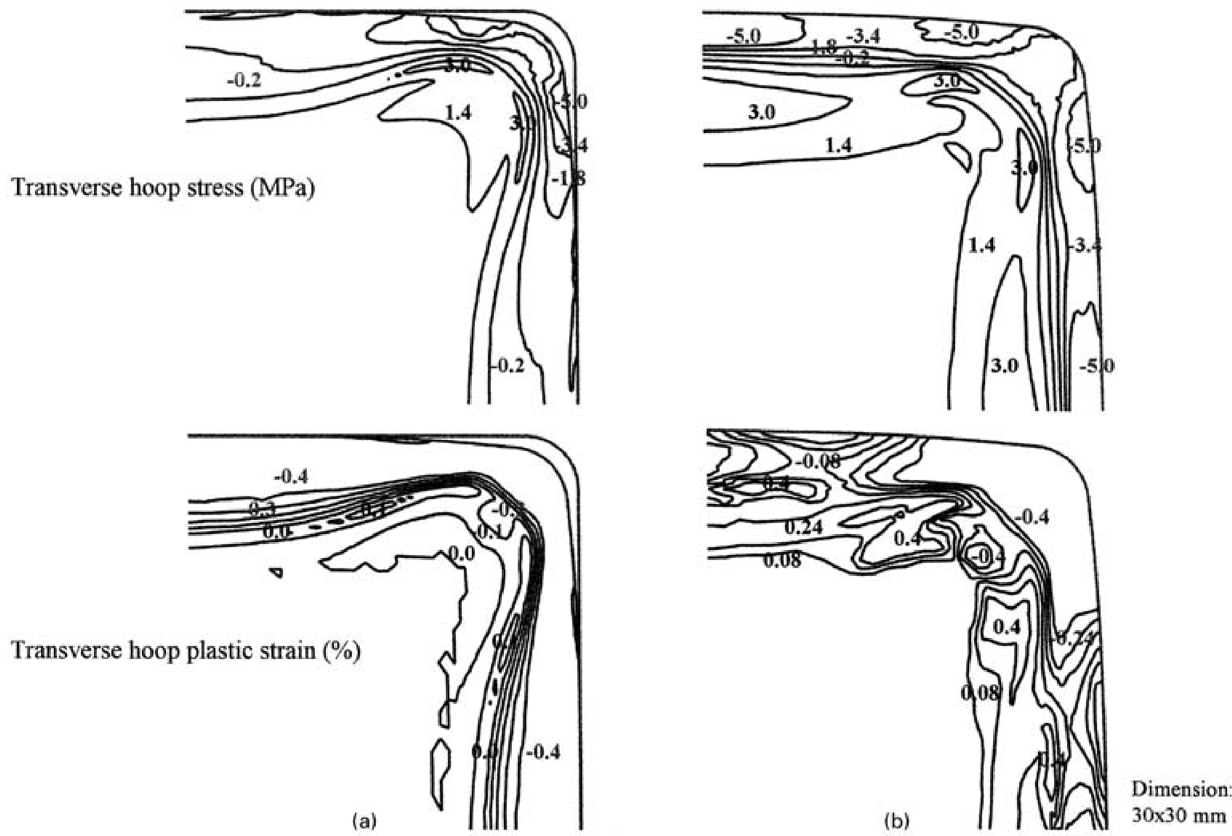

a mould exit; *b* 100 mm below mould

23 Hoop stress and hoop plastic strain contours for 4 mm corner radius: oil casting

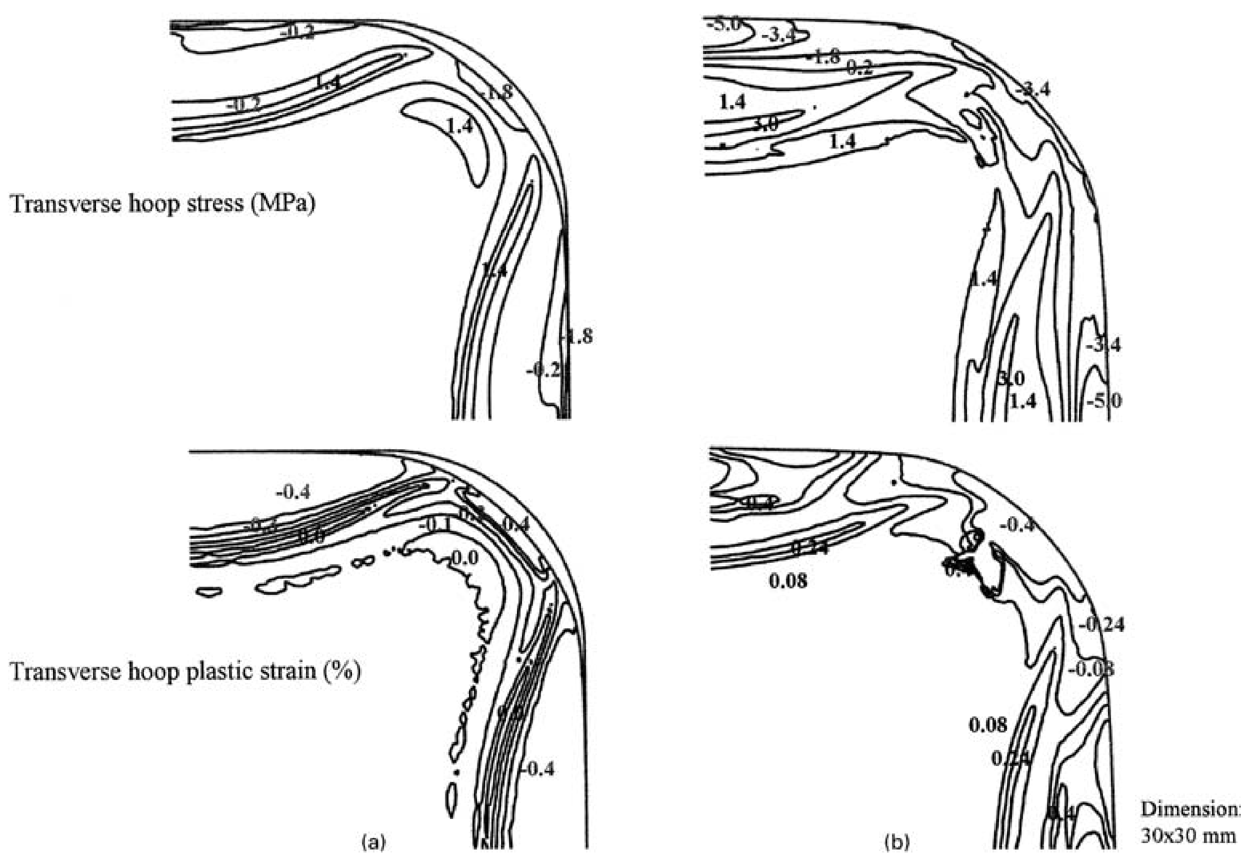

a mould exit; *b* 100 mm below mould

24 Hoop stress and hoop plastic strain contours for 15 mm corner radius: oil casting

ias0001675 23-09-02 11:50:50 Rev 14.05
The Charlesworth Group, Huddersfield 01484 517077

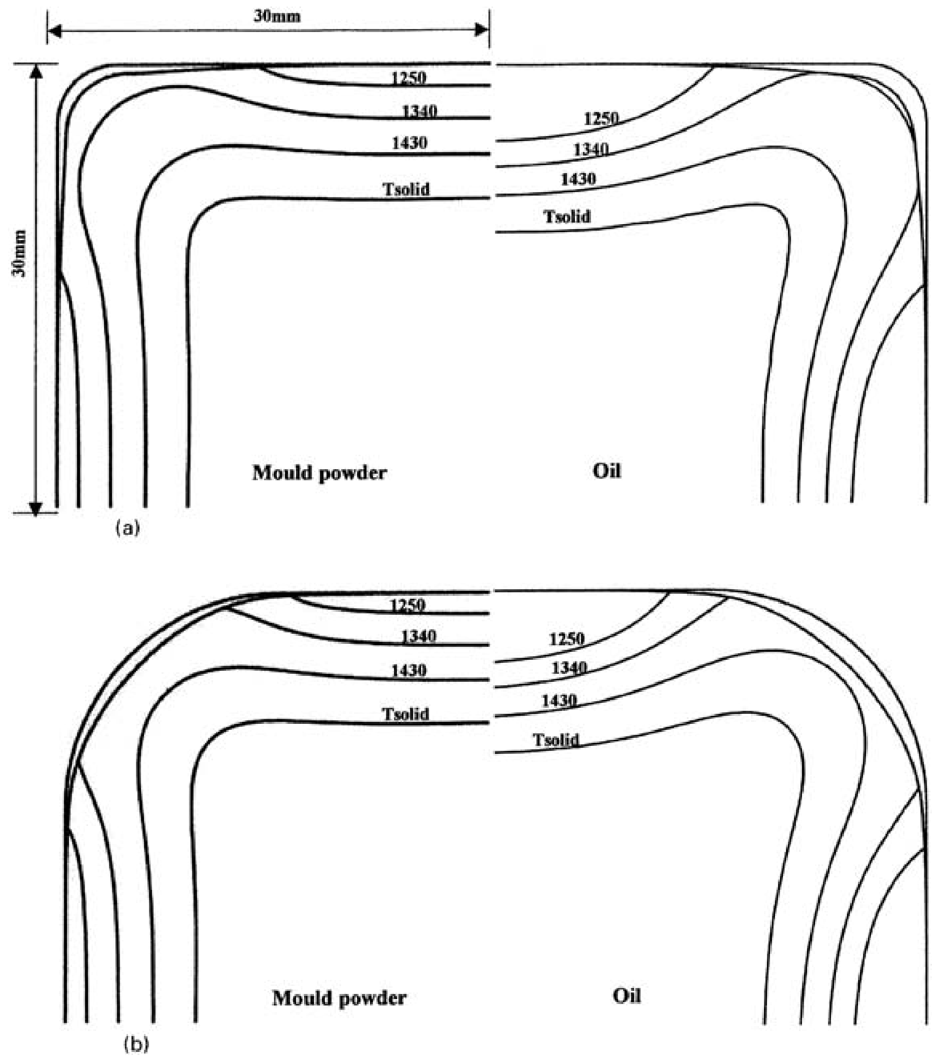

a 4 mm corner radius; *b* 15 mm corner radius

25 Comparison of solid shell contours at mould exit with given lubricants and corner radius

In the present analysis, the flux layer is assumed to maintain constant thickness during gap formation. In reality, it is likely that liquid flux will build up to fill the gap. This would increase the corner heat flux relative to the predictions here, which would give rise to even more uniform shell thickness. Therefore, for the same average heat flux and shell thickness at the mould exit, the powder casting practice is expected to be less susceptible to cracks, owing to better uniformity of the solidifying shell.

MECHANISM OF LONGITUDINAL CRACK FORMATION

The numerical analysis carried out in the present study indicates two distinct mechanisms to generate longitudinal corner cracks or longitudinal off corner internal cracks in the casting of steel billets with inadequate linear taper. Longitudinal corner cracks are predicted to arise only in large corner radius billets, owing to tension developing across the hotter and thinner shell along the exact centre of the corner during solidification in the mould. Such surface cracks could extend deeper because of solid shell bulging both in the mould, owing to mould wear, or below, owing to poor alignment of the guide rolls. On the other hand, small corner radius billets allow the formation of a thinner shell at the off corner region inside the mould. This exacerbates the hinging action that accompanies bulging below the mould. This causes high plastic tensile strain across the dendrites in the off corner region, leading to longitudinal subsurface off corner cracks in billets cast in these moulds.

Although the above analysis ignores the important effects of asymmetry, rhomboidity phenomena, and lower ductility from copper pickup on these defects, these mechanisms suggest more about mould operation. Applying mould powder as the lubricant allows the shell to solidify more uniformly, which could potentially reduce both of these types of cracks. Employing an optimised parabolic mould taper could achieve the same benefit. Mould wear effectively reduces the taper and probably worsens both cracking problems. Mould wear at the corner would cause a more severe gap, leading to a hotter and thinner shell there, which would increase susceptibility to corner surface cracks. Mould wear at the centre would allow billet bulging to occur inside the mould. This could allow the hinge action inside the mould, and increase susceptibility to off corner subsurface cracks. Misaligned or missing guide rolls would also aggravate the below mould bulging and hinging mechanism.

Finally, the present work suggests that mould corner radius controls how longitudinal cracks are manifested, but is not the root cause of the problem. This means that large corner radius moulds could be used effectively to improve smooth rolling operations while still maintaining quality billets free of longitudinal cracks, as long as other casting parameters are optimised. Specifically, an optimised parabolic mould taper should be employed together with a well maintained mould shape (free of wear and permanent distortion),

ias0001675 23-09-02 11:50:50 Rev 14.05
The Charlesworth Group, Huddersfield 01484 517077

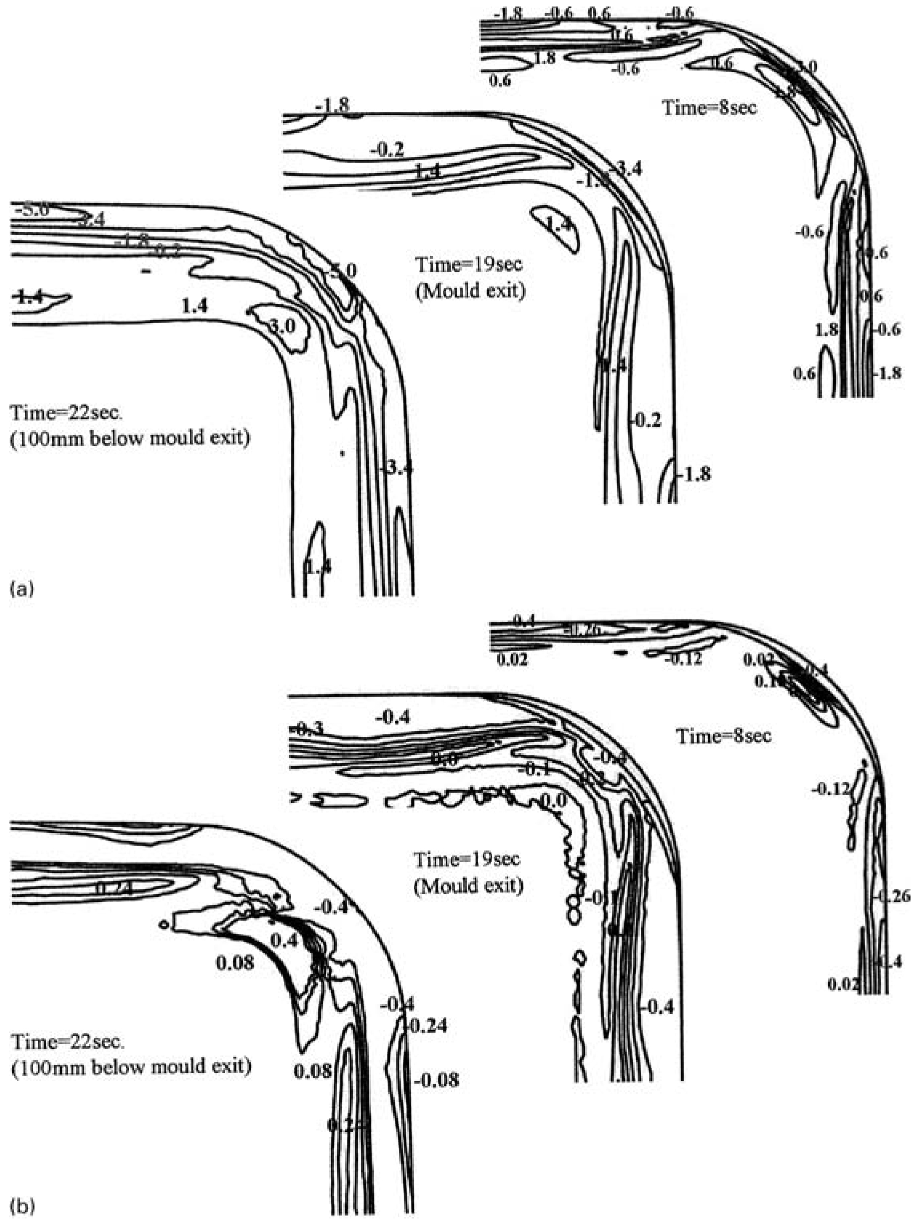

a hoop stress; *b* hoop plastic strain

26 Evolution of calculated stress and strain contours for 15 mm corner radius with powder casting

mould powder lubrication, and adequately aligned foot rolls. More study is needed to achieve these requirements for different casting speeds, section sizes, and mould lengths.

CONCLUSION

Using a two-dimensional coupled thermoelastoviscoplastic finite element model of a slice through the continuous cast strand, the thermomechanical behaviour of a square billet has been analysed. Calculated results of temperature of the mould, heat flux, thickness of the solidifying shell, bulging deformation, and location of longitudinal crack formation are in good agreement with experimental observations. The following conclusions are based on simulations of 4 mm and 15 mm radius corners of 120 mm square billets of low carbon steel with only 0·75%/m linear taper and cast at 2·2 m min^{-1}.

1. A gap forms in the corner region of linear taper moulds owing to insufficient taper.

2. As the corner radius of the billet increases from 4 to 15 mm, this gap spreads further around the corner towards the centre of the strand and becomes larger. The accompanying drop in heat flux leads to more non-uniformity in temperature around the billet perimeter as solidification proceeds.

3. Longitudinal corner cracks are predicted only in the large corner radius billet. They form as a result of tension within the hotter and thinner shell along the corner during solidification in the mould (150–520 mm down the mould). These surface cracks could extend deeper by solid shell bulging owing to mould wear, or poor alignment of guide rolls below the mould.

4. Longitudinal off corner subsurface cracks are predicted to form more easily in the small corner radius billet. They are caused by hinging of the thin, weak shell around the corner at the off corner region, as a result of bulging allowed either in the mould by mould wear, or below the mould by poor guide roll alignment.

5. Changing from oil lubrication to powder casting with good infiltration and high gap conductivity and/or optimising mould taper leads to a more uniform shell in the mould, with potential benefits for reducing longitudinal cracks.

ias0001675 23-09-02 11:50:50 Rev 14.05
The Charlesworth Group, Huddersfield 01484 517077

6. With optimised parabolic taper, no mould wear, proper powder lubrication, and adequate submould guide roll support, large corner radius billets should be castable without longitudinal cracks, with the benefit of a smoother corner for rolling operations.

APPENDIX

The gap size of 4 mm and 15 mm corner radius moulds for casting 120 mm square billets was approximated geometrically assuming:

(i) shrinkage is 0·5%

(ii) circumferential length of the gap is 11·78 mm ($\pi \times 15/4$ mm).

Figure 27*a* shows a schematic diagram of the corner region of a 15 mm radius billet, where $\overline{BF}$ is the initial radius (15 mm), $\overline{AF} = \overline{AD}$ is the new radius, $\overline{EF}$ is the initial half perimeter of the 15 mm radius, and $\overline{DF}$ is the new half perimeter of the new radius.

From Fig. 27*a*, the following relationships can be obtained

$$\frac{\theta}{\sin\theta} = \frac{\overline{EF}(1 - 0{\cdot}5\%)}{\overline{BF}\sin 45} \quad (12)$$

$$\overline{AF} = \overline{AD} = \frac{\overline{BF}\sin 45}{\sin\theta} \quad (13)$$

$$\overline{AB} = \overline{AF}\cos\theta - \overline{BF}\cos 45 \quad (14)$$

From equations (12)–(14), the gap size for a 15 mm radius billet, $\overline{DE} = \overline{AB} + 15 - \overline{AD}$, is found to be 1·3 mm.

Figure 27*b* shows the corner region of a 4 mm radius billet. Assuming the same circumferential gap length, the billet perimeter can be divided into three parts, a straight part $\overline{FG}$, an angled part $\overline{FH}$, and the 4 mm radius part as indicated.

The new half perimeter $\overline{FG} + \overline{FI} + \overline{ID}$ is 0·5% less than the initial half perimeter $\overline{GHE}$, expressed by

$$\overline{FG} + (\overline{FH} + \overline{HI})^{1/2} + \frac{\pi}{4}(\overline{BE} - \overline{DE}) = \overline{FHE}(1 - 0{\cdot}5\%) \quad (15)$$

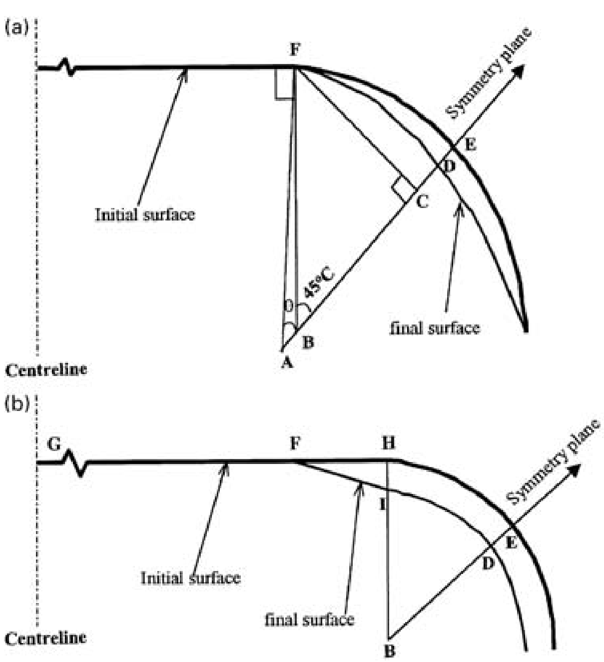

a 15 mm corner radius; *b* 4 mm corner radius

27 Schematic diagrams of billet corner regions

Solving equation (15), the gap size $\overline{DE} = \overline{HI}$ for a 4 mm radius billet is 0·79 mm.

ACKNOWLEDGEMENTS

The authors would like to acknowledge the financial and technical support of POSCO. They would also like to thank Professor K. H. Oh (Seoul National University) for permission to use the model discussed here. The authors are also grateful for the support of Dr T. J. Yeo (formerly post-doctorial at University of British Columbia) and Y. Meng (graduate student at University of Illinois) in the model development. Mr J. Shaver (graduate student at University of British Columbia) is also thanked for helpful discussion. Support of one of the authors (BGT) from the Continuous Casting Consortium at the University of Illinois, the National Science Foundation (Grant DMI 98–00274), and the National Center for Supercomputing Applications at UIUC is also acknowledged.

REFERENCES

1. Y. AKETA and K. USHIJIMA: *Tetsu-to-Hagané*, **46**, 1733–1740.
2. Y. AKETA and K. USHIJIMA: *Tetsu-to-Hagané Overseas (J. Iron Steel Inst. Jpn)*, 1962, **2**, 334–343.
3. J. K. BRIMACOMBE, F. WEINBERG, and E. B. HAWBOLT: *Can. Metall. Q*, 1980, **19**, 215–227.
4. I. V. SAMARASEKERA, J. K. BRIMACOMBE, and K. WILDER: *Iron Steelmaker*, March, 1994, 1–13.
5. R. HAURI: Proc. Symp. on 'Advances in continuous casting research', Cairo, Egypt, April, 1992, 291–298.
6. A. GRILL, J. K. BRIMACOMBE, and F. WEIBERG: *Ironmaking Steelmaking*, 1976, **3**, 38–47.
7. K. SORIMACHI and J. K. BRIMACOMBE: *Ironmaking Steelmaking,* 1977, **4**, 240–245.
8. J. O. KRISTIANSSON: *J. Therm. Stress.*, 1982, **5**, 315–330.
9. J. O. KRISTIANSSON and E. H. ZETTERLUND: *J. Therm. Stress.*, 1984, **7**, 209–226.
10. J. E. KELLY, K. P. MICHALEK, T. G. O'CONNOR, B. G. THOMAS, and J. A. DANTZIG: *Metall. Trans. A*, 1988, **19A**, 2589–2602.
11. T. C. TSZENG, Y. T. IM, and S. KOBAYACHI: *Int. J. Mach. Tools Manuf.*, 1989, **29**, 107–120.
12. I. V. SAMARASEKERA and J. K. BRIMACOMBE: *Metall Trans. B*, **13B**, 1982, 105–116.
13. C. CHOW: Master's thesis, University of British Columbia, Vancouver, Canada, 2001.
14. V. P. PERMINOV, N. M. LAPOTYSHKIN, V. E. GIRSKII, and A. I. CHIZHIKOV: *Stal'*, 1968, **7**, 560–563.
15. H. MORI: *Tetsu-to-Hagané (J Iron Steel Inst. Jpn)*, 1972, **58**, 1511–1525.
16. W. P. YOUNG and W. T. WHITFIELD: *Open Hearth Proc.*, 1968, **51**, 127–132.
17. K. MATSUNAGA: *Open Hearth Proc.*, 1976, **59**, 228–248.
18. Y. AKETA and K. USHIJIMA: *Tetsu-to-Hagané*, 1959, **45**, 1314–1345.
19. I. OHNAKA and Y. YASHIMA: Proc. Int. Conf. on 'Modeling of casting and welding processes', 1998, Vol. 4, 385–394.
20. K. H. KIM, Y. G. LEE, H. N. HAN, K. H. OH, and D. N. LEE: Proc. Conf. on 'Modeling of casting and solidification process', 1995, 37–50.
21. Y. M. WON, T. J. YEO, K. H. OH, J. K. PARK, J. CHOI, and C. H. YIM: *ISIJ Int.*, 1998, **38**, 53–62.
22. B. G. YOU, S. H. LEE, D. N. LEE, U. S. YOON, and Y. K. SHIN: Proc. Conf. on 'Modeling of casting and solidification process', 1991, 101–112.
23. K. KIM: PhD thesis, Seoul National University, Seoul, Korea, 1996.
24. Y. UESHIMA, S. MIZOGUCHI, T. MATSUMIYA, and H. KAJIOKA: *Metall. Trans. B*, 1986, **17B**, 845–859.
25. Y. M. WON, T. J. YEO, D. J. SEOL, and J. H. OH: *Metall. Trans. B*, 2000, **31B**, 779–794.
26. E. A. MIZIKAR: *Trans. AIME*, 1967, **239**, 1747–1753.
27. B. LALLY, L. BIEGLER, and H. HENEIN: *Metall. Trans. B*, 1990, **21B**, 761–770.
28. A. YAMAUCHI, K. SORIMACHI, T. SAKURAYA, and T. FUJII: *ISIJ Int.*, 1993, **33**, 140–147.

29. W. R. STORKMAN: Master's thesis, University of Illinois, Urbana, IL, USA, 1990.
30. J. K. BRIMACOMBE, P. K. AGARWAL, S. HIBINS, B. PRABHAKER, and L. A. BAPTISTA: 'Continuous casting', Vol. 2, 109–123; 1984, ISSM.
31. F. P. INCROPERA and D. P. DEWITT: 'Fundamental's of heat transfer', 401; 1981, New York, Wiley.
32. B. G. THOMAS, B. HO, and G. LI: Proc. 1998 McLean Symp., 1998, 177–193.
33. Y. MENG and B. G. THOMAS: Unpublished report, July 2001.
34. P. J. WRAY: in 'Modeling of casting and welding processes', (ed. H. D. Apelian and H. D. Brody), 245–257; 1980, Warrendale, PA, TMS-AIME.
35. H. N. HAN, Y. G. LEE, K. KIM, K. H. OH, and D. N. LEE: *Mater. Sci. Eng. A*, 1996, **A206,** 81–89.
36. K. KIM, Y. LEE, H. N. HAN, K. H. OH, and D. N. LEE: *Ironmaking Steelmaking*, 1997, **24**, 249–256.
37. K. J. SEOL, Y. M. WON, T. J. YEO, K. H. OH, J. K. PARK, and C. H. YIM: *ISIJ Int*., 1999, **39**, 91–98.
38. K. KINOSHITA, T. EMI, and M. KASAI: *Tetsu-to-Hagané (J. Iron Steel Inst. Jpn)*, 1979, **65**, 2022–2031.
39. 'AMEC2D manual', Seoul National University, Seoul, Korea, 1996.
40. K. KAWAKAMI, T. KIRAGAWA, K. MURAKAMI, Y. MIYASHITA, Y. TSUCHIDA, and T. KAWAWA: *Nippon Kokan Tech. Rep*., 1983, **93**, 1493.
41. J. H. WEINER and B. A. BOLEY: *J. Mech. Phys. Solids*, 1963, **11**, 145–154.
42. A. MOITRA: PhD thesis, University of Illinois, Urbana, IL, USA, 1993.
43. A. MOITRA, B. G. THOMAS, and H. ZHU: *ISS Steelmaking Conf. Proc*., 1993, **76**, 657–667.
44. A. WANG, B. N. WALKER, and I. V. SAMARASEKERA: *Can. Metall. Q*., 2000, **39**, 441–454.
45. J. FU: Master's thesis, University of British Columbia, Vancouver, Canada, 2001.
46. C. A. M. PINHEIRO, I. V. SAMARASEKERA, J. K. BRIMACOMBE, and B. N. WALKER: *Ironmaking Steelmaking*, 2000, **27**, 37–54.